https://doi.org/10.5194/egusphere-2025-5691
Preprint. Discussion started: 8 December 2025

Thaw slump erosion accelerates fluvial sediment transport after a heatwave on the Taymyr Peninsula, Russia

Evan N. Dethier[1], Christian M. Erikson[2], Carl E. Renshaw[3]

[1]Department of Earth Sciences, Colby College, Waterville, ME, 04901, United States of America
[2]GFZ Helmholtz Centre for Geosciences, Potsdam, 14473, Germany
[3]Department of Earth Sciences, Dartmouth College, Hanover, 03755, United States of America

Correspondence to: Evan N. Dethier (edethier@colby.edu)

Abstract. Thaw slumps appear to be expanding across much of the Arctic, yet questions remain about the catalysts for failure, as well as the quantity and fate of sediment eroded from these mass-wasting features, its role in downstream material transport, and how erosion evolves after initial failure. Here, we document the watershed-scale consequences of the largest single-initiation thaw slump event to date, which covers more than 30,000 km² on the Taymyr Peninsula in northern Russia. Using automated satellite methods, we track the rapid failure of more than 1,700 individual thaw slumps and record their ongoing post-failure erosion. We use a combination of Landsat and Sentinel-2 data to show that suspended sediment concentrations (SSC) downstream of slump clusters spiked to 2–5x background levels immediately (1–2 days) after the acceleration of thaw slump failure during the 2020 Siberian heat wave. Elevated suspended sediment transport rates scale with the upstream density of slumps and have persisted as slumps continue to erode; sediment transport during the period 2020–2024 is thus unprecedented in the region during the 40-year Landsat record. Although elevated relative to pre-failure, sediment export to the ocean appears to be significantly less than what is transported by rivers into estuaries, suggesting that estuarine storage may account for much of the eroded lost material, potentially transforming estuarine physical processes and altering aquatic habitat.

1 Introduction

As Arctic environments respond to climate warming, a central question has emerged: will rates of hillslope and fluvial erosion change (Fields et al., 2025; Lininger and Wohl, 2019; Zhang et al., 2022)? Despite increasing attention in the past decade, scientists have not yet reached a consensus on this topic; researchers have found evidence both for increasing erosion (Erikson et al., 2025; Fields et al., 2025; Geyman et al., 2024; Lantz and Kokelj, 2008; Rowland et al., 2023), decreasing erosion (Ielpi et al., 2023), and evidence of non-uniform, watershed-specific change (Dethier et al., 2022). Erosion could decrease if vegetation growth is bolstered by warmer temperatures; resulting increases in root strength could increase sediment cohesion, leading to slower hillslope processes, fewer mass failure events, and slower rates of riverbank erosion (Ielpi et al., 2023). Conversely, erosion could increase if other processes outpace vegetation-mediated cohesion. In particular, permafrost, which is stabilized by frozen water content, may lose the indurating effect of ice as it thaws, potentially increasing hillslope erosion, mass failure rates, and riverbank erosion, with consequences for human infrastructure (Hjort et al., 2018) and ecology (Newcombe and Macdonald, 1991).

An indicator of increased warming-driven erosion is the occurrence of mass failures in permafrost sediments, commonly known as “retrogressive thaw slumps”. These failures, which we simply call “thaw slumps”, are closely associated with rising temperatures (Bernhard et al., 2022a; Dai et al., 2025; Erikson et al., 2025; Lantz and Kokelj, 2008; Lewkowicz and Way, 2019) and are thought to result from permafrost thaw, particularly the melting of ice lenses that stabilize otherwise unconsolidated sediments (Jiao et al., 2025). Increased precipitation has also been identified as a potential catalyst for failure (Burn and Lewkowicz, 1990; Kokelj et al., 2015). Thaw slumps have been observed throughout the Arctic but exhibit a non-uniform spatial distribution, primarily occurring in areas of thick permafrost near former glacial margins (Dai et al., 2025).

Measurements of the timing of slump initiation are limited to a small number of studies, which generally report increases in slump initiation during the satellite record (Bernhard et al., 2022a; Dai et al., 2025; Lantz and Kokelj, 2008; Lewkowicz and Way, 2019; Maier et al., 2025). Fewer studies have documented the transmission of slump-eroded sediment, with some reporting on individual slumps (Erikson et al., 2025; Kokelj et al., 2013, 2015, 2021) or using qualitative assessments of color changes in sediment-laden waters (Lewkowicz and Way, 2019). Studies of downstream sediment transport have similarly been confined to limited regions or timeframes (Kokelj et al., 2013, 2015, 2021), or inferred indirectly based on slump-erosion measurements for larger regions with multiple slumps (Bernhard et al., 2022a). Notably, only Erikson et al. (2025) has directly measured sediment transport changes before and after slump initiation, and this study focused on a single slump. Thus, the full picture of thaw slump failure timing, erosion progression, and downstream sediment transport consequences remains uncertain, particularly on a regional basis. Improving knowledge of the factors controlling slump failure, progressive erosion, and sediment transport is essential to advancing our understanding of Arctic erosion dynamics.

Advances in satellite imagery and processing techniques have greatly enhanced our ability to study thaw slumps, enabling automated detection of slump occurrence and timing, tracking of progressive slump failure after initiation (Erikson et al., 2025), and estimation of suspended sediment transport in rivers (Dethier et al., 2020, 2022). Building on previous efforts that documented individual thaw slump initiation, erosion, and sediment delivery, we analyze over 1,700 thaw slumps on the Taymyr Peninsula, Russia (Fig. 1), most of which initiated during a regional heatwave in 2020 (DeAngelis et al., 2023) and have been previously documented by Bernhard et al., (2022a) and Bernhard et al., (2022b). Using satellite imagery from multiple sensors, we track progressive erosion since initial failure. We ask whether slumps contribute measurable sediment to affected rivers and, if so, whether sediment contributions scale with increases in slump footprint. In light of observed increases in slump activity, we also explore whether slump-derived sediment leads to measurable increases in sediment export to the ocean or whether it is retained within riverine and estuarine sinks.

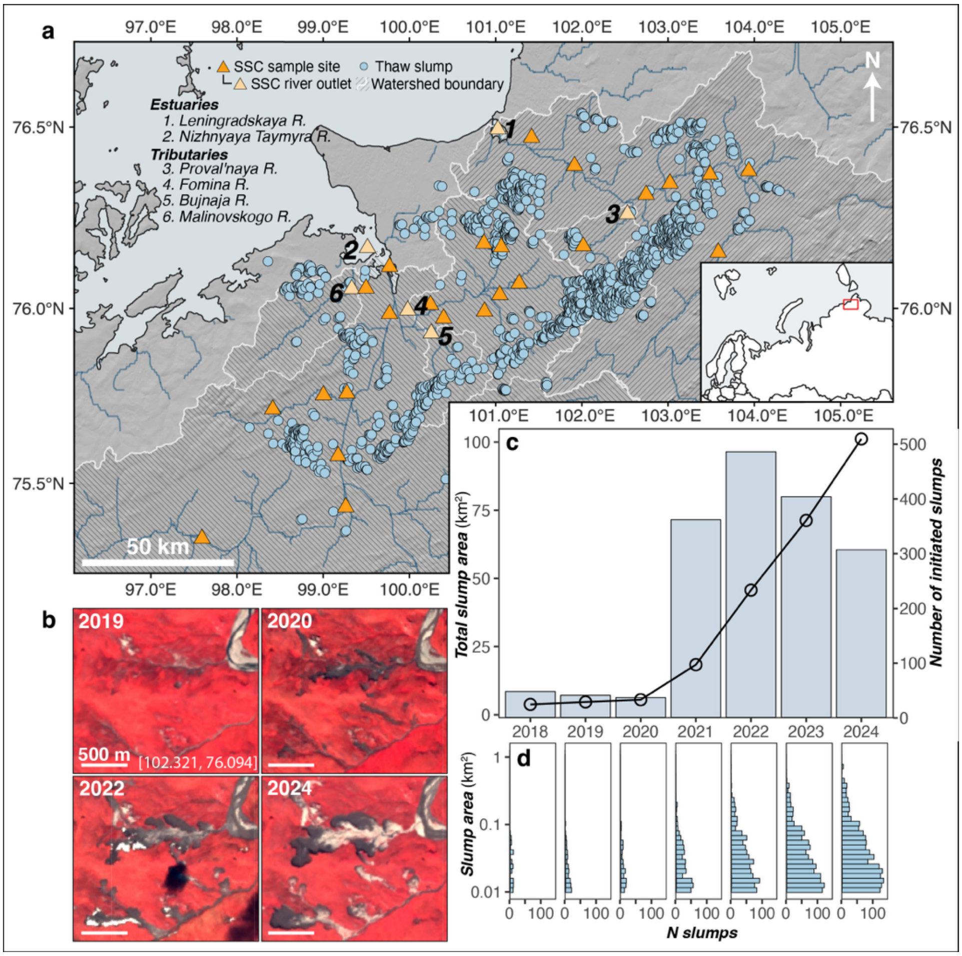

Figure 1: Slumps occur pervasively on the Taymyr Peninsula, Russia and have increased their total footprint 20-fold since 2020. a, Slump locations (blue) and sampling locations (orange: sample station; numbered and shown light orange: river outlet sample station) are shown within the study watersheds (white outlines) on map of the study region in Taymyr Peninsula Russia. Watersheds that drain into the Leningradskaya River and Nizhnyaya Taymyra River, respectively, have hash shading in opposite directions. b, An example of slump expansion from 2019–2024 in the Proval'naya R. watershed is shown with Sentinel-2 images (false color; R,G,B: near-infrared, red, green). c, The number of slumps and total slump area increased dramatically during the study period, as did average slump area, d, as new small slumps failed and existing slumps expanded. Note that pixels must be classified as "slump" in 60% of images in a year to qualify as a slump for that year, so slump initiation in c was no later than that year. The x-axis showing year in c also indicates the year for the corresponding panel in d, below.

https://doi.org/10.5194/egusphere-2025-5691
Preprint. Discussion started: 8 December 2025

2 Methods

We based our analysis on a suite of remote-sensing methods using Landsat 5, 7, 8, and 9 (Tier 1, Level 2 surface reflectance; subsequently referred to as “Landsat") and Sentinel-2 Multispectral Instrument (Level 1-C, top-of-atmosphere radiance; subsequently referred to as “Sentinel-2”) data to detect thaw slump occurrence, monitor slump growth, and assess downstream impacts on suspended sediment transport. We contextualized these measurements using climate estimates provided by the ERA5 reanalysis product (Copernicus Climate Change Service, Climate Data Store, 2023). Detailed descriptions of the methods for each objective are provided below, and all analyses are fully reproducible with code archived in a permanent repository.

2.1 Detecting slumps using Landsat and Sentinel-2 imagery

Our automated methods for detecting and measuring erosion depend on repeat satellite imagery from 1985–2024. Thaw slumps are visible in this imagery, but detection is challenging due to variability in slump and landscape spectral characteristics, both in time and space. To address these complexities, we implemented a tiered procedure for slump detection and planform area analysis, with initial identification of slump zones using Landsat data (Tier 1), refinement of slump planform extent in 2024 using higher spatial- and temporal-resolution Sentinel-2 data (Tier 2), and slump expansion from 2018–2024 analyzed using Sentinel-2 data (Tier 3).

To identify slump zones (Tier 1), we used 30-meter resolution Landsat surface reflectance data spanning 1985–2024, from Landsat 5 through Landsat 9. Each image was preprocessed to remove clouds, water bodies, and artifacts. We created a warm-season composite image by taking the pixelwise median of all the processed images from each of five multi-year epochs: 1985–1990, 1995–2000, 2005–2010, 2015–2020, and 2022–2025. From the most recent available epoch (usually 2022–2024), we identified local spectral anomalies indicative of slumping via nearest-neighbor pixel analysis, capitalizing on the spectral contrast between slumps and surrounding terrain. A pixel was identified as anomalous if it exceeded by more than 120% the median “greenness” and “brownness” of pixels within 900 meters. For these anomalous pixels, we calculated temporal linear trends in vegetation “greenness” and “brownness” indices across the five epochs. We eliminated pixels with non-significant trends or connected pixel groupings less than 200 m^2, with the remaining pixels identified as potential slumps. We then sampled all the Landsat data for these potential-slump pixel clusters and conducted a second round of elimination based on trend analysis for day-of-year groups (i.e., seasons), requiring that trends show consistent change in at least two such groups. This approach limited the false-positive rate to 5% (190 out of 200 slumps correctly identified in a manual inspection of a subset).

To increase the slump inventory and slump segmentation detail, we used data from the Sentinel-2 Multispectral Instrument (2016–present) (Tier 2: slump delineation), which provides medium resolution in space (10 m pixel resolution for bands used in this analysis) and time (< 5 day return period). The shorter operational period of Sentinel-2 limits long-term timeseries analysis. However, relatively few slumps existed in the region in 2018 (n=47), suggesting that this shorter record is sufficient for evaluating slump growth. The goal of this step was mostly to limit omissions of slumps from the Landsat-derived dataset; these occurred primarily due to strict temporal trend thresholds, the spatial and temporal resolution limits of Landsat data, and occasional spectral confusion with non-slump features. We trained a random forest model to identify slumps in Sentinel-2 data, labeling Sentinel-2 images from 2024 as "slump" or "not slump" using the slump extents from our Landsat-based slump analysis. After confirming model accuracy with a holdout test set (98.2% correct identification based on a 20% holdout set), we applied the random forest model to all the Sentinel-2 images from 2024, limiting the application to pixels within 500 m of a Landsat-identified slump polygon. Cloud cover, snow, and other image-to-image inconsistencies necessitated additional quality control for this pixel-wise classification, so we only categorized a pixel as "slump" if it was identified as a slump in >60% of images from 2024.

We set the Sentinel-2-derived slump area from the 2024 analysis as a maximum slump extent for subsequent annual segmentation of each slump in the 2024 inventory. For each year from 2018–2023, we then applied the random forest model to each image of each slump. Just as for 2024, to be classified as a slump in a given year we required that a pixel be identified as slump in >60% of that year's images (see above, Tier 2). Each polygon thus captures the maximum extent from the year prior, as late-season slump growth would not be recorded by 60% of that year's images. The output from this process is a dataset of slump-extent polygons, allowing us to track slump growth over time. We summarized progressive slump growth for a) each slump, b) each watershed for our suspended sediment analysis (see below), and c) in aggregate for the study region.

2.2 SSC analysis

To assess the impact of thaw slump activity on suspended sediment transport, we combined Landsat surface reflectance data (Level 2, Collection 2, Tier 1) with Sentinel-2 top-of-atmosphere (TOA) radiance data (Level 1-C). Landsat provides a multi-decadal record (1984–present) that enables long-term contextualization of SSC changes following slump events, albeit at moderate spatial (30 m) and temporal (16-day revisit) resolution. In contrast, Sentinel-2 offers higher spatial resolution (10 m) and more frequent observations (daily to sub-weekly), but over a shorter timeframe (2016–present). The seasonal availability of imagery is comparable between sensors and consistent across pre- and post-slump periods (Fig. A1). Leveraging the complementary strengths of both datasets, we constructed a four-decade SSC time series with the relatively infrequent Landsat data, supplemented by a detailed recent Sentinel-2 record.

SSC sampling locations along rivers and estuaries were manually selected based on Sentinel-2 imagery, focusing on slump-affected rivers wide enough for both Landsat and Sentinel-2 SSC estimates. Generally, these river widths exceed 60 m. Although this approaches the lower limit for accurate Landsat-based SSC estimation, particularly in clear-water systems, elevated post-slump SSC values justified analysis even at these narrower sites (Dethier, 2023). Our final sampling network included non-tidal river stations within four watersheds (Malinovskogo: 2 stations; Fomina: 7; Proval'naya: 2; Bujnaja: 1) and two estuaries (Leningradskaya: 6; Nizhnyaya Taymyr: 5), as well as four control stations with limited slump activity (Fig. 1). Table 1 details the number of satellite-derived SSC observations acquired at each location. Additionally, we extracted SSC measurements at 1-km intervals along manually delineated transects through the two estuaries using Sentinel-2 data.

Table 1. Summary of stations where suspended sediment concentration was estimated using algorithms developed for Landsat 5, 7, 8, and 9 and Sentinel-2 satellites.

River	**Lat.**	**Long.**	**Changepoint date**	**Watershed area (km^2)**	**Slump area (km^2)**	**% Slump area**	**Landsat dates**		**Sentinel-2 dates**	
							Ref.	**Post-slump**	**Ref.**	**Post-slump**
Malinovskogo	76.054	99.331	***8/4/20***	799	1.4	0.172	79	40	74	187
Malinovskogo	76.056	99.497	***8/4/20***	840	1.5	0.179	94	31	40	104
Fomina	76.181	100.865	***8/4/20***	295	0.9	0.299	67	32	33	78
Fomina	76.171	101.065	***8/4/20***	320	1.2	0.384	80	63	36	73
Fomina	76.069	101.273	8/11/20	474	9.1	1.923	72	37	73	188
Fomina	76.037	101.048	***8/5/20***	610	4.0	0.654	70	56	42	108
Fomina	75.991	100.871	***8/4/20***	1,349	14.0	1.04	75	51	45	100
Fomina	75.972	100.397	***8/5/20***	1,948	16.2	0.833	106	67	30	81
Fomina	76.010	100.244	***8/4/20***	1,964	16.2	0.826	107	73	32	88
Fomina	75.994	99.981	***8/4/20***	2,547	20.0	0.786	106	72	35	82
Proval'naya	76.173	102.017	***8/4/20***	353	11.6	3.294	75	30	84	175
Proval'naya	76.278	102.626	***8/4/20***	570	11.9	2.079	75	43	74	196
Bujnaja	75.930	100.253	***8/4/20***	438	3.8	0.864	91	61	29	78
Leningradskaya	76.371	103.489	8/29/20	8,286	8.2	0.099	89	13	39	116
Leningradskaya	76.347	103.023	8/16/20	8,761	13.3	0.152	79	30	89	206
Leningradskaya	76.316	102.746	8/23/20	9,709	35.8	0.369	90	41	81	231
Leningradskaya	76.395	101.915	***8/5/20***	10,692	37.3	0.349	89	10	67	197
Leningradskaya	76.471	101.417	***8/5/20***	10,910	38.7	0.355	74	15	113	354
Leningradskaya	76.494	101.027	***8/5/20***	11,269	39.4	0.35	66	9	83	222
Nizhnyaya Taymyra	75.579	99.173	7/18/20	120,419	5.8	0.005	100	8	72	133
Nizhnyaya Taymyra	75.759	99.275	8/23/20	121,958	11.5	0.009	92	4	66	161

River	**Lat.**	**Long.**	**Changepoint date**	**Watershed area (km^2)**	**Slump area (km^2)**	**% Slump area**	**Landsat dates**		**Sentinel-2 dates**	
							Ref.	**Post-slump**	**Ref.**	**Post-slump**
Nizhnyaya Taymyra	75.984	99.769	9/4/20	122,671	13.0	0.011	87	3	35	97
Nizhnyaya Taymyra	76.116	99.769	***8/5/20***	125,311	32.1	0.026	82	5	33	102
Nizhnyaya Taymyra	76.169	99.514	6/29/20	126,448	34.5	0.027	82	3	39	104
Control	76.381	103.937	***8/3/20***	3,190	0.3	0.009	83	-	39	104
Control	76.156	103.584	8/23/20	3,679	3.6	0.099	95	-	30	76
Control	75.338	97.594	7/18/20	14,685	0.0	0	106	-	32	68
Control	74.161	98.361	8/15/20	45,747	0.0	0	99	-	37	89

To prepare data for SSC estimation, we applied a series of preprocessing steps at each sampling location for every image. Clouds were masked using the Landsat FMask algorithm (from quality control bands) or the Sentinel-2 Cloud Probability dataset. Water pixels were identified using a modified normalized-difference water index (NDWI) with thresholds of 0 for Landsat and 0.1 for Sentinel-2, based on Green and SWIR1 bands; slightly different thresholds for the different sensors were chosen to ensure consistency in water extent, given variations in spectral range for bands from the respective sensors. Areas with slopes exceeding 8 m/m (derived from ArcticDEM) were excluded to avoid non-water surfaces. Additional brightness and quality control filters masked snow, ice, non-water pixels, and image artifacts. To take a sample for SSC analysis, we calculated the median pixel value within a 200-meter radius of the sampling station and recorded the number of pixels used in this calculation.

Landsat data can be used to estimate SSC using established algorithms (Dethier, 2019; 2020; 2022; 2023). These algorithms enhance accuracy by classifying rivers into six major "types" via k-means clustering, following Dethier (2019), rather than applying a single global model. Typical uncertainties are approximately a factor of two (relative fractional error ~0.71). These models have been generated using global training data, including some from Arctic rivers, primarily in Canada. To generate Sentinel-2 SSC estimates, we developed a region-specific model by pairing 1,356 Sentinel-2 samples with temporally and spatially coincident Landsat-derived SSC values. Using this dataset, we performed a multiple linear regression to derive an SSC estimation algorithm for Sentinel-2 data, allowing SSC estimates consistent with Landsat-derived values for the study area (Fig. A2) and enabling direct cross-sensor comparison. We used Sentinel-2 TOA data, rather than surface reflectance, due to the shorter period of record for the Sentinel-2 surface reflectance product (available only since 2019) and some unresolved issues with river edges in turbid water.

For each station, we constructed timeseries of SSC using Landsat data. We also calculated upstream slump area, both absolute (km^2) and normalized by watershed area (% slump area, km^2/km^2) to facilitate comparisons among watersheds. We evaluated seasonal and annual SSC variations before and after 2020 across individual stations, watersheds, and river types. To enable consistent comparison across stations, we computed SSC anomalies, defined as the difference between annual SSC and the pre-2020 average SSC (SSC anomaly = SSC annual – pre-2020 average SSC).

To assess transmission of slump-derived sediment to rivers, we compared annual SSC to the prior year's % slump area. We used this one-year lag because our slump delineation requires that pixels have a "slump" designation in 60% of the images from a given year; late-season slump growth, as occurred when many slumps initiated in late 2020, is thus not captured until the following year. We evaluated downstream trends in watersheds with multiple stations, as well as in the estuaries, to test for SSC attenuation due to deposition. To test the generality of SSC–% slump area scaling, we grouped stations in the same watershed to generate a watershed-wide relationship between SSC anomaly and % slump area. We also tested whether this relationship had region-wide generality by combining all station measurements together, excluding those from control reaches.

2.2.1 Improved accuracy likely with local calibration

The suspended sediment concentration (SSC) estimates derived from Landsat and Sentinel-2 algorithms in this study have not been locally calibrated using in-situ samples from the study region. Global error assessments for these remote sensing methods suggest that SSC estimates are generally accurate within a factor of two relative to actual concentrations in similar river systems, with potential improvements arising from the temporal averaging applied here. Comparable accuracy was reported by Erikson et al. (2025), using independent estimates of slump-derived sediment inputs to an affected river.

While erosion volume estimates for thaw slumps exist for this area (Bernhard et al., 2022b), a key limitation is the absence of local discharge data necessary to convert SSC into sediment flux, as Erikson et al. (2025) did using a long-term discharge record from a nearby river. Region or river-specific measurements of discharge would be a welcome addition to analysis of these sensitive systems, particularly if coupled with ecogeomorphic evaluations from the field. Due to limited field access to this potential study region, however, we rely for now on remote measurements of SSC calibrated with a broadly distributed training dataset.

2.2.2 Slump initiation test using Sentinel-2-derived SSC data

To evaluate whether slump failures induced temporally consistent changes in sediment concentration across the study region, we analyzed the 2020 timeseries of Sentinel-2-derived SSC data, which offers sub-weekly to daily temporal resolution, depending on cloudiness. For each river and estuarine sampling station, including control sites, we performed change point detection on the SSC time series using the `cpt.mean` function from the *R* Changepoint package. This analysis identified

https://doi.org/10.5194/egusphere-2025-5691
Preprint. Discussion started: 8 December 2025

statistically significant shifts in mean SSC and the timing of these shifts at each location, including control stations and estuaries.

2.3 Temperature and precipitation analysis

We obtained daily estimates of temperature, precipitation, and snow depth from 1950 to 2024 for the study region, using the ERA5 climate reanalysis dataset. We calculated the annual average daily maximum temperature (*TMax*) and assessed temporal trends over this period. To characterize temperature extremes, we fit a normal distribution to annual average maximum daily temperatures and computed the probability of observing each year's average *TMax* within the distribution. We also calculated the probability of the 2020 average annual *TMax* for a set of periods; each period ended in 2024 and we varied the start year from 1950–2000. We also tested probability across this set of periods with 2020 excluded.

We contextualized the 2020 temperature, precipitation, and snowpack on a seasonal basis. For the years 1950–2024 we calculated the average maximum temperature for each day of the year (Day 1 = January 1st, Day-of-year 365 = December 31st). We calculated the anomaly from that average for each day in 2020. We analyzed daily precipitation to identify departures from normal conditions, with particular focus on an early August 2020 event when an estimated 14 mm of precipitation fell on the region. To assess the extremity of this event, we computed single-day and three-day running precipitation totals for all summer months from 1950 to 2024 and estimated the probability of observing a similar event.

3 Results

3.1 Thaw slumps initiated in 2020 and continued eroding

Following the 2020 Siberian heatwave, thaw slump activity surged in the study area. By 2021, 361 new thaw slumps had formed, with an additional 485 confirmed by 2022. The total thaw slump area expanded steadily from 3.7 km² in 2018 to 101.1 km² by 2024. Measures of slump size have all increased roughly linearly since 2020, including total area, maximum individual slump area, and median slump area. While the total slump area shows early signs of leveling off by 2024, the limited time span makes it premature to draw firm conclusions about this potential attenuation.

Table 2. Summary of the number of slumps and total slump area, by year. Note that slumps must have been present in 60% of a year's images to be assigned to that year, so the record of slump initiation may lag actual initiation by 1 year.

Year	Total slump area (km^2)	Increase in slump area (km^2)	Avg. slump area (km^2)	Initiated slumps	Total slumps
2018	3.8	-	0.081	47	47
2019	4.7	0.9	0.054	40	87
2020	5.5	0.8	0.045	36	123
2021	18.4	12.9	0.038	361	484
2022	45.7	27.3	0.047	485	969
2023	71.2	25.5	0.052	403	1,372
2024	101.1	29.9	0.060	306	1,678

3.2 Thaw slumps have increased river suspended sediment transport

Using suspended sediment concentration (SSC) algorithms developed for Landsat data, we detect significant ($p < 0.05$) increases in SSC downstream of thaw slumps (Fig. 2). These increases range from 2 to 5 times background levels in affected non-tidal rivers, with an average increase of 3.45 ± 0.91 SD (Fig. A3). The 40-year SSC record for slump-impacted rivers reveals that this sustained sediment input following the 2020 slump event is unprecedented in recent history, with potentially substantial implications for physical and ecological processes. Elevated SSC levels persisted through at least 2024 in affected rivers and estuaries (Fig. 3). While some control rivers exhibited SSC increases during 2020–2021, possibly related to heatwave-driven erosion absent slump activity, they generally did not sustain elevated levels beyond this period (Fig. 3c).

SSC increases occurred immediately following widespread thaw slump erosion in 2020 (Fig. 2, insets) and have persisted through the study period ending September 2024. Although these trends are apparent in Landsat data, the Landsat mission's relatively limited temporal resolution limits determination of the precise timing of initiation. Changepoint analysis of the more temporally dense Sentinel-2 SSC time series reveals strong regional coherence in the timing of SSC increases (Fig. A4, Table 1). This analysis indicates that the Taymyr landscape may have shifted to a higher erosion regime in as little as 1–2 days: SSC increased at 10 stations on Aug. 4, 2020 and an additional 6 stations on Aug. 5th, accounting for 16 of 24 non-control stations. Control rivers do not exhibit a temporally coherent increase in SSC during 2020 (Fig. A4).

Of the eight stations with a different changepoint, seven are located in the upper estuaries of the Nizhnyaya Taymyra and Leningradskaya Rivers, upstream of most slump-affected tributaries. Stations in those estuaries that are directly downstream of slump-affected tributaries have changepoints of August 4th and 5th. Sentinel-2 imagery coverage was relatively even throughout 2020 season, with usable images on 65% of days between June 29 and September 15, indicating that the regional coherence is not an artifact of sampling bias.

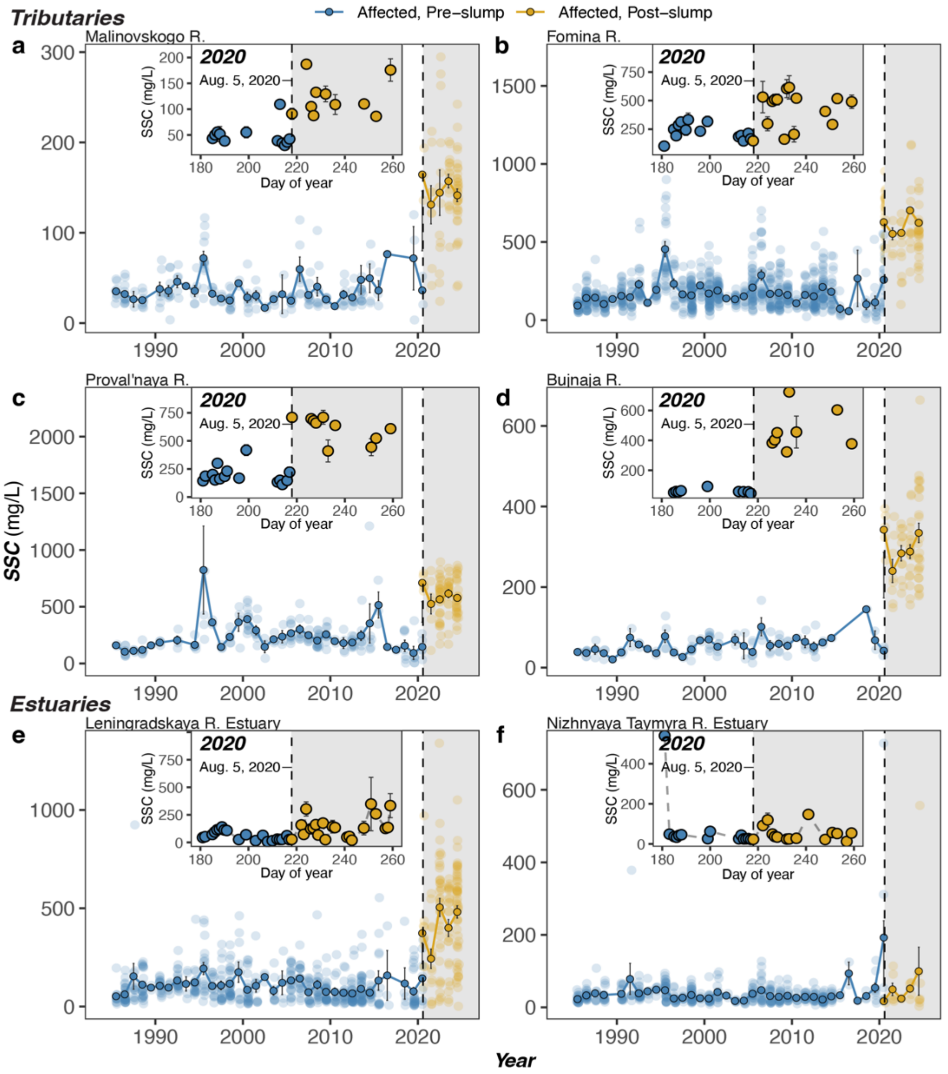

Figure 2. Suspended sediment concentration (SSC) increased downstream of thaw slumps initiated in 2020 for rivers on the Taymyr Peninsula, Russia. Each panel in the plot shows data for all stations along one river, with transparent points showing all measurements, solid outlined points showing annual averages with error bars (95% confidence interval). Symbol color indicates samples from pre-2020 (affected, pre-slump: blue) and post-2020 (affected, post-slump: yellow). Increase in SSC at tributary rivers (a–d), and the Leningradskaya R. Estuary (e) is statistically significant ($p < 0.05$). Changes in SSC are not statistically significant in the Nizhnyaya Taymyra R. Estuary (f).

https://doi.org/10.5194/egusphere-2025-5691
Preprint. Discussion started: 8 December 2025

In non-tidal rivers affected by thaw slump activity, we find that suspended sediment transport scales with upstream slump area ($p < 0.05$) (Fig. 3) and has continued to rise in response to ongoing slump occurrence and expansion since 2020 (e.g., Fig. 2b–d). At individual river sampling sites, slump area is a significant predictor of average annual SSC in 8 of 12 non-tidal rivers, and marginally significant in two additional sites ($p = 0.099$ and $p = 0.102$, respectively, for stations on the Malinovskogo R. tributary). For rivers exhibiting significant slump area–SSC relationships, slump area explains 59–91% of the SSC variance from 2018 to 2024 (Fig. A5). Percent slump area is a stronger predictor of SSC in watersheds where a larger proportion of the basin is affected ($p < 0.001$) (Fig. A6); 13 of 14 stations with > 0.3% upstream slump area have significant correlations between slump extent and SSC.

This positive scaling between slump area and SSC is consistent within individual watersheds. In four of five watersheds with multiple sampling stations, the SSC anomaly (annual SSC – pre-2020 average SSC) is significantly correlated with percent upstream slump area ($p < 0.05$), accounting for 52–72% of the annual SSC variance in those watersheds (Fig. 3a,b). Despite some variability among watersheds, this relationship appears broadly generalizable across the region (Fig. A7). Specifically, a tenfold increase in percent slump area corresponds to an average SSC increase of approximately 131 mg/L (±14 mg/L standard error; $R^2 = 0.36$, $p < 0.001$). Restricting analysis to watersheds with more than 0.01% slump area strengthens the signal, yielding an SSC increase of 231 mg/L per tenfold increase in slump area (±22 mg/L standard error; $R^2 = 0.47$, $p < 0.001$) (Fig. A7).

https://doi.org/10.5194/egusphere-2025-5691
Preprint. Discussion started: 8 December 2025

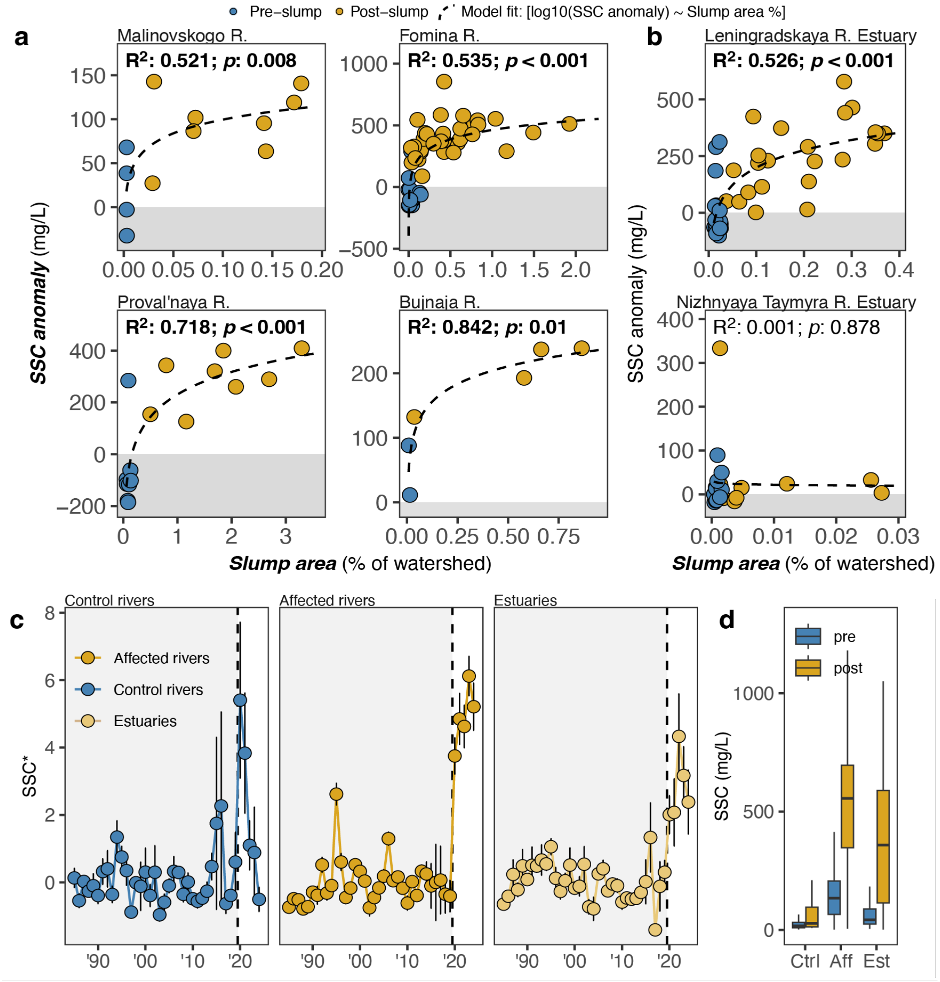

Figure 3. SSC increased in affected rivers and estuaries after thaw slumps occurred in 2020. Annual average SSC anomaly (SSC–average – pre-slump SSC) scales with upstream percent slump area for rivers, a, and estuaries, b, affected by thaw slumps on the Taymyr Peninsula, Russia (2018–2020: blue symbols; post-2020: yellow symbols). Each panel shows SSC anomaly values for one river; each symbol is from one year at an individual satellite sampling station. The dashed line on each panel is a least-squares fit relating the SSC anomaly to the log-transformed percent slump area in the upstream watershed for all measurements along that river. The relationship R^2 and *p*-value is shown at the top of each panel, bolded if significant ($p < 0.05$). Points falling in the grey shaded area are below the pre-slump mean SSC c, Timeseries of annual standardized SSC (SSC*: standard deviations from the 1984–2019 annual-averaged mean) for control rivers, slump-affected rivers, and estuaries in the study region show the changes after 2020 (vertical dashed line). d, The absolute magnitude of SSC increase varied in these different categories, with SSC highest in rivers affected by thaw slumps, both before and after 2020.

3.3 Estuaries have elevated SSC, but trap much of the slump-derived suspended sediment

Slump-affected tributary rivers deliver significantly elevated suspended sediment concentrations (SSC) to the Taymyr-region estuaries during the warm season; however, much of this sediment appears to be retained within the estuarine systems. Both Landsat and Sentinel-2 analyses show that upstream of slump-affected tributary inflows, SSC values are statistically indistinguishable from pre-slump baseline levels (Leningradskaya R. Estuary: Fig. 4c, hashed area; Nizhnyaya Taymyra R.

Estuary: Fig. A8b, hashed area). In each estuary, SSC spikes to peak levels downstream of the first slump-impacted tributary (Fig. 4c). In the Leningradskaya R. Estuary, elevated SSC is sustained by further tributary inputs between 80 km and 20 km from the estuary mouth. Conversely, the slump-affected Fomina River in the Nizhnyaya Taymyra Estuary produces a lower SSC peak, likely reflecting dilution effects arising from the much larger watershed area of the Nizhnyaya Taymyra River (122,671 km²) compared to the Leningradskaya River (8,761 km²) at their respective first slump-affected tributary confluences. Upstream of the Fomina R. confluence, very few thaw slumps are present, so the Fomina R. SSC inputs to the Nizhnyaya Taymyra R. are strongly diluted by clear water. Qualitative observations of river color also support these quantitative findings of changes in time and patterns along estuaries (Fig. 4b, Figs. A8–A9).

Downstream of the last major slump-affected tributary, SSC declines steadily to the mouth of the estuaries. In the Leningradskaya R. Estuary, this decline begins approximately 30 km from the mouth, decreasing by roughly 5 mg/L per kilometer to reach 43% of the peak SSC at the estuary outlet. The decline continues offshore as the sediment plume is dispersed and, likely, deposited (Fig. 4c). In contrast, SSC in the Nizhnyaya Taymyra R. Estuary decreases more gradually at a rate of 0.6 mg/L per kilometer, beginning 45 km upstream from the mouth near the Fomina River and reaching approximately 70% of the peak value at the ocean boundary.

The relationship between SSC and upstream percent slump area in the Leningradskaya Estuary also indicates substantial estuarine sediment trapping. Upstream of the first major slump-affected tributary, SSC shows a positive but statistically non-significant correlation with slump area ($p = 0.23$) (Fig. A5e). Below this tributary, the relationship strengthens markedly and remains significant across four monitoring stations, explaining 64–90% of the annual SSC variance from 2018 to 2024 ($p =$ 0.01, <0.01, 0.03, <0.01, respectively). At the estuary outlet station, however, the correlation dissipates ($p = 0.94$), indicating that upstream slump area no longer influences SSC leaving the estuary, despite an upstream slump extent exceeding 0.3%.

https://doi.org/10.5194/egusphere-2025-5691
Preprint. Discussion started: 8 December 2025

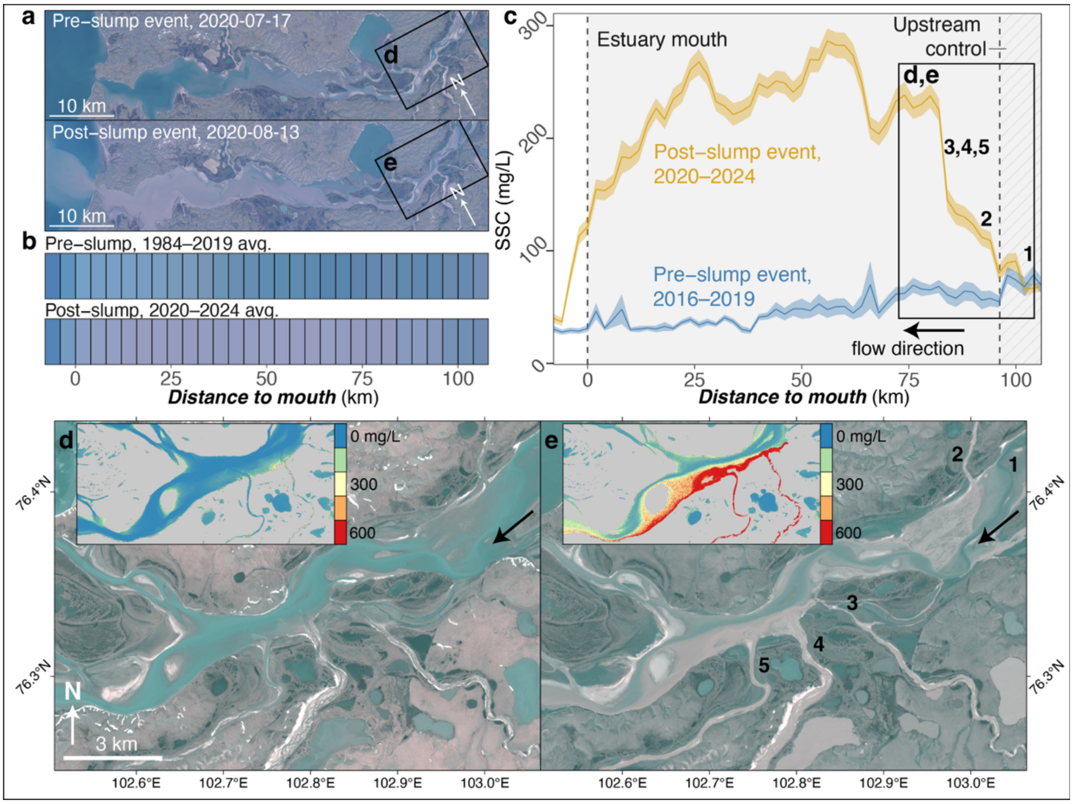

Figure 4. Estuaries indicate peak sediment transport just downstream of slump-affected tributaries, with attenuation downstream of these inputs. Qualitative imagery analysis (a) shows limited SSC in the Leningradskaya River Estuary pre-slump event in July 2020 and increased SSC immediately post-slump event in August 2020, including a sediment plume exiting the estuary and entering the open ocean. Aggregate analysis of average Landsat image color every 4 km in the estuary (b) also indicates limited pre-slump estuarine SSC from 1984–2019 (darker colors), and elevated SSC post-slump from 2020–2024 (lighter colors), but shows a clear darkening near the estuary mouth even post-slump. Quantitative SSC analysis based on Sentinel-2 images (c) also shows this attenuation near the estuary mouth, with peak SSC driven by tributary inputs and less than 50% of the peak mid-estuary SSC exiting the estuary. Tributary inputs are elevated downstream of slump areas, with low contributions in pre-slump 2016 imagery (d) and much higher inputs post-slump in 2020 (e). Insets in d and e show spatially explicit SSC estimates for the main images. The extent window in a approximately corresponds to the distance scale in b. The area covered in d and e is shown in boxes in a and c. Tributary inputs numbered in e are indicated for reference in c. Flow direction is indicated in c, d and e, from right to left (east to west).

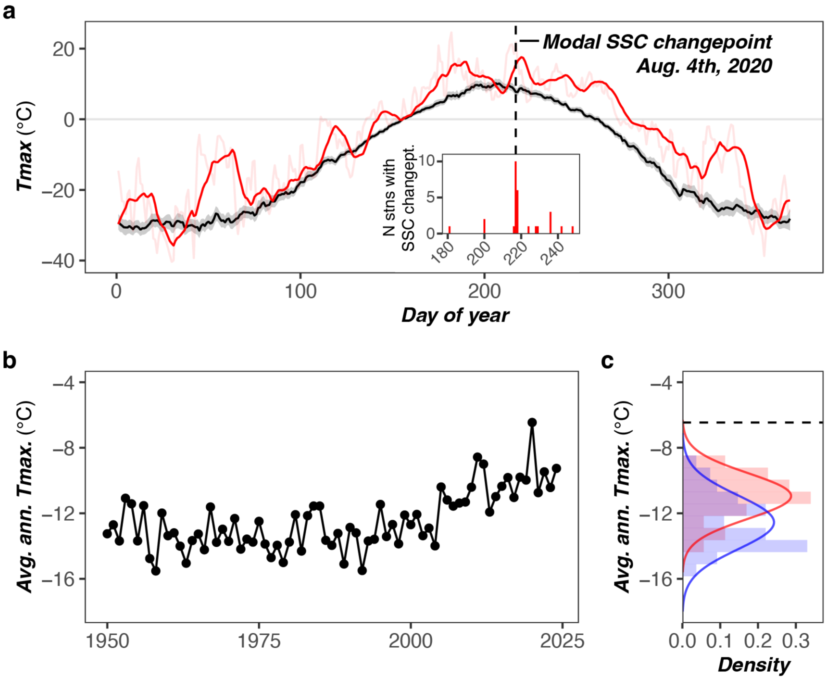

Figure 5. Temperatures during the 2020 thaw slump event were anomalously high on the Taymyr Peninsula, Russia. a, Average maximum temperatures for 1950–2024 for each day of year are shown (mean: black, grey shading: 95% confidence interval), compared to temperatures during 2020 (red: 10-day running average, pale red: daily). b, average annual temperature, calculated from maximum daily temperature, shows a decadal trend toward warming. The 2020 annual average of -6.45°C is an outlier even recently, as shown in c, a histogram of annual temperatures from 1950–2000 (blue) compared to 2000–2024 (red, 2020 not shown), with probability density functions with a normal distribution fit to each period. The 2020 annual average temperature (dashed line, y-intercept = -6.45°C) had a 1/3880 probability of occurrence based on a normal distribution fitting the full record, exclusive of 2020. Note that histograms in c have been normalized to a density scale for easier comparison.

3.4 Thaw slump failure and SSC increase coincided with the 2020 Siberian heat wave

The widespread thaw slump failures in 2020 occurred concurrently with a sustained warm period during the 2020 Siberian heatwave (Fig. 5). Our analysis of ERA5 Land data reveals that the annual average maximum temperature in 2020 was –6.45°C, more than 6°C above the long-term average of –12.55°C (±1.64 SD for 1950–2024, excluding 2020). This temperature anomaly corresponds to an estimated recurrence interval of approximately 1 in 3,880 years based on historical data, excluding 2020 itself (Fig. A10). While stationarity assumptions underlying these statistics may be violated due to recent warming trends (evidenced by the shifted temperature distribution in Fig. 5**b** and 5**c**), these estimates highlight that such extreme heat events have become increasingly likely over time.

A marked increase in SSC and peak in thaw slump erosion rates occurred on August 4–5, coinciding with a brief but intense warm spell within the longer heatwave period (Fig. 5a). Three extremely warm days occurred during this period: August 1st, 2nd, 4th were the 49th, 44th, and 28th warmest days since 1950 in the region. Between August 2 and 4, 14 mm of rain also fell.

This amount of rainfall, although uncommon, has occurred regularly since 2000 in the study area and had already occurred during 2020 prior to August 4th–5th (Fig. A11). On average there are 8.3 warm-season days per year with a 3-day precipitation total of 14 mm or greater (n = 200 days, 2020–2024), and 1.2 days per year with a single-day total of 14 mm or greater (n = 28 days, 2020–2024).

Snowfall, similarly, shows some departure from normal, with lower peak snowfall depth and earlier-than-normal melting (Fig. A12). However, most snow was melted from the study area by the end of June, 2020, more than a month before region-wide acceleration in slump erosion.

4 Discussion

4.1 Thaw slumps contribute to non-uniform geomorphic change in the Arctic

The rapid expansion of thaw slumps on the Taymyr Peninsula, Russia, underscores a growing trend of accelerating geomorphic change in the Arctic (Fields et al., 2025; Geyman et al., 2024). The 2020 slump event generated a clear and predictable increase in suspended sediment with direct implications for downstream sediment flux and water quality. Qualitative observations confirm that most slumps are hydrologically connected to local streams or lakes, facilitating the efficient transfer of failed sediment to river networks. The region-wide, synchronous increase in SSC beginning in early August, 2020 coincides with initial slump activity, highlighting the strong coupling between thaw slump erosion and fluvial sediment transport. As thaw slump initiation and expansion continue across Arctic landscapes, sediment flux and associated ecological effects in affected watersheds are likely to intensify.

Unexpectedly, some control sites also exhibited elevated SSC in 2020, albeit with less temporal coherence than slump-impacted watersheds. This suggests the 2020 warm season may have induced region-wide increases in sediment delivery, potentially through enhanced bank erosion driven by warming (Fields et al., 2025; Geyman et al., 2024). Although it is possible that undetected slumps occurred in control basins, manual inspections reveal few, if any, such features triggered by the 2020 heatwave. Additionally, SSC in these control rivers returned near baseline levels after 2021 (Fig. 3c). These observations suggest that while thaw slumps provide an acute indicator of warming-driven geomorphic change, warming impacts on sediment transport extend beyond slump-affected watersheds. In some cases, slumps may be an acute or leading indicator of broader impacts.

4.2 Thaw slump failure and SSC increase has become more likely as temperatures have warmed

Spatial variability in Arctic geomorphic change may reflect heterogeneity in the pace and magnitude of regional warming. Thaw slump erosion is known to be highly temperature sensitive (e.g., Erikson et al., 2025), consistent with broader patterns of accelerated Arctic erosion (Fields et al., 2025; Geyman et al., 2024). The unprecedented 2020 heatwave may have crossed critical thermal thresholds, triggering widespread slump initiation akin to events observed elsewhere. For example, Banks Island, Canada, experienced thousands of thaw slumps at densities comparable to those documented here (Lewkowicz and Way, 2019). However, initiation timing of thaw slumps in that region is less constrained, so it is difficult to determine whether slumps were initiated by one or more warming events. Lewkowitz and Way (2019) found that it was likely the cumulative effect of multiple warm years, rather than a single event trigger, consistent with results elsewhere in the Arctic (Dai et al., 2025; Lantz and Kokelj, 2008).

On the Taymyr Peninsula, it is likely that failure in 2020 was also made more likely by the cumulative effect of many warm years since 2004 (Fig. 6), as well as a warm winter and spring. However, the initiation and rapid acceleration of so many slumps in a matter of days, rather than years, and at the peak warmth of a season-long heat wave, points to the importance of the acute, short-lived warming event between August 1–4, 2020. A precipitation event may also have played a role: qualitative assessments from satellite imagery suggest that rainfall on August 2–4, 2020 was followed by an increase in river discharge, although no quantitative discharge data are available for this region. Given that the rainfall and discharge do not appear to be particularly uncommon magnitudes, we believe it unlikely that precipitation was the sole catalyst for this increase in erosion. However, we cannot yet definitively attribute erosion increases to warming alone, nor establish the relative contributions of permafrost melt, rainfall, and potential undercutting by high flows.

Whether such abrupt responses are generalizable across other Arctic slump-prone regions requires further investigation. Enhanced understanding of failure dynamics is essential to establish the influence of extreme heat events on permafrost degradation.

High temporal-resolution monitoring of fluvial SSC, as demonstrated here using satellite data, offers promise for early detection of thaw slump activity. The immediate increase in SSC following initial slump failure in 2020 suggests that river SSC may be the most sensitive indicator of such acute upstream change. The use of SSC to detect watershed disturbance has been suggested or used in other monitoring applications, notably for mining onset (Dethier, 2022; 2023), and also for a single thaw slump in Northwest Territories, Canada (Erikson, 2025), but has not been shown with the to-the-day specificity we are able to achieve here. Because rivers integrate upstream watershed signals, SSC monitoring requires only a limited number of strategically placed stations, simplifying operational logistics and reducing computational overhead for remote sensing analyses. This obviates the need for total watershed image processing, limiting remote-sensing computational needs and allowing resources to be focused on follow-up study after a change in SSC has been detected. This straightforward approach can also be applied easily to other regions. Although region-specific SSC calibration improves absolute measurement accuracy (Dethier et al., 2020), our findings suggest that relative change detection is robust even with minimal calibration, facilitating broader application.

4.3 Storage in estuaries may limit sediment transmission to the ocean

The trapping of slump-derived sediment by estuaries, reducing the signal of increased sediment transport to the ocean (see below), may contribute to the lack of consensus on the geomorphic effects of Arctic warming. We find that the two estuaries in the study area attenuate the signal of slump erosion, with SSC decreasing steadily from the downstream-most confluence with a slump-affected tributary to the estuary mouth (Fig. 4c, Fig. A8). Estuaries are depositional features, so this result is unsurprising. Still, we note that the estuaries appear to have increased annual storage to accommodate increased sediment influx, aggrading rather than simply transporting these additional loads.

We estimate that approximately 50% of the sediment from slump-affected rivers has exited the estuaries to the ocean. Large plumes of sediment are present in some warm-season satellite images, beginning immediately after slump failure in 2020 (Fig. 4a, lower panel), suggesting that river inputs exceed estuarine trapping for some events (Rodriguez et al., 2020), but turbid waters in the estuary often do not make it to the mouth. Because our satellite-based algorithms are not trained on estuarine waters, it is possible that the estuaries are exporting more sediment than we are measuring, although others have had success monitoring estuarine sediment transport using similar methods (Luo et al., 2022). It is also possible that accommodation space in the estuaries will be exhausted by elevated sediment loads and export will become more efficient in coming years (Slagle et al., 2006). However, for now our analysis indicates that estuaries are an important filter on upstream changes to sediment flux, potentially dampening the transmission of continental signals to global oceans.

5 Conclusion

To date, changes in riverine suspended sediment concentrations and fluxes have not been a leading indicator of climate change (Dethier et al., 2022). Rather, the largest alterations in sediment transport have resulted from human activities, such as reductions due dam construction or increases due to alluvial mining (Dethier et al., 2022, 2023). The failure of these thaw slumps shows that order-of-magnitude changes are also possible due to climate warming.

The rapid and extensive slump initiation on the Taymyr Peninsula, preceded by limited prior thaw slump failure, suggests that thaw slump susceptibility may be more widespread than previously recognized. It is important to assess the preconditions necessary for thaw slump failure, including permafrost presence, sediment thickness, and antecedent warming. In addition, better understanding the key catalysts for this event, and whether particular underlying geology made it more likely on the Taymyr Peninsula than other permafrost zones, remains a topic of pressing importance. For instance, what were the relative roles of a decade of warm temperatures, an historically warm year, and an extreme, short-duration heat event? Although still rare, such heatwaves have become more likely on the Taymyr Peninsula (DeAngelis et al., 2023) consistent with increases in likelihood across the Arctic (Perkins-Kirkpatrick and Lewis, 2020; Rantanen et al., 2024). Should Arctic permafrost be susceptible to similar failures elsewhere, Arctic rivers may transform faster than expected, potentially in a matter of days.

Although much of the Arctic has experienced rising temperatures and changing hydrology, researchers have not reached consensus on the occurrence or likelihood of resulting geomorphic change. The lack of detectable change could be because expected erosion increases are offset by other shifts in watershed processes. Detectable geomorphic changes may also lag climatic changes due to buffered or noisy processes. In this work, we add to a growing body of evidence that detectable changes are ongoing; improvement in the development and deployment of monitoring, analytical, and theoretical tools will likely uncover more changes and detect them sooner after they occur.

5 Appendix A

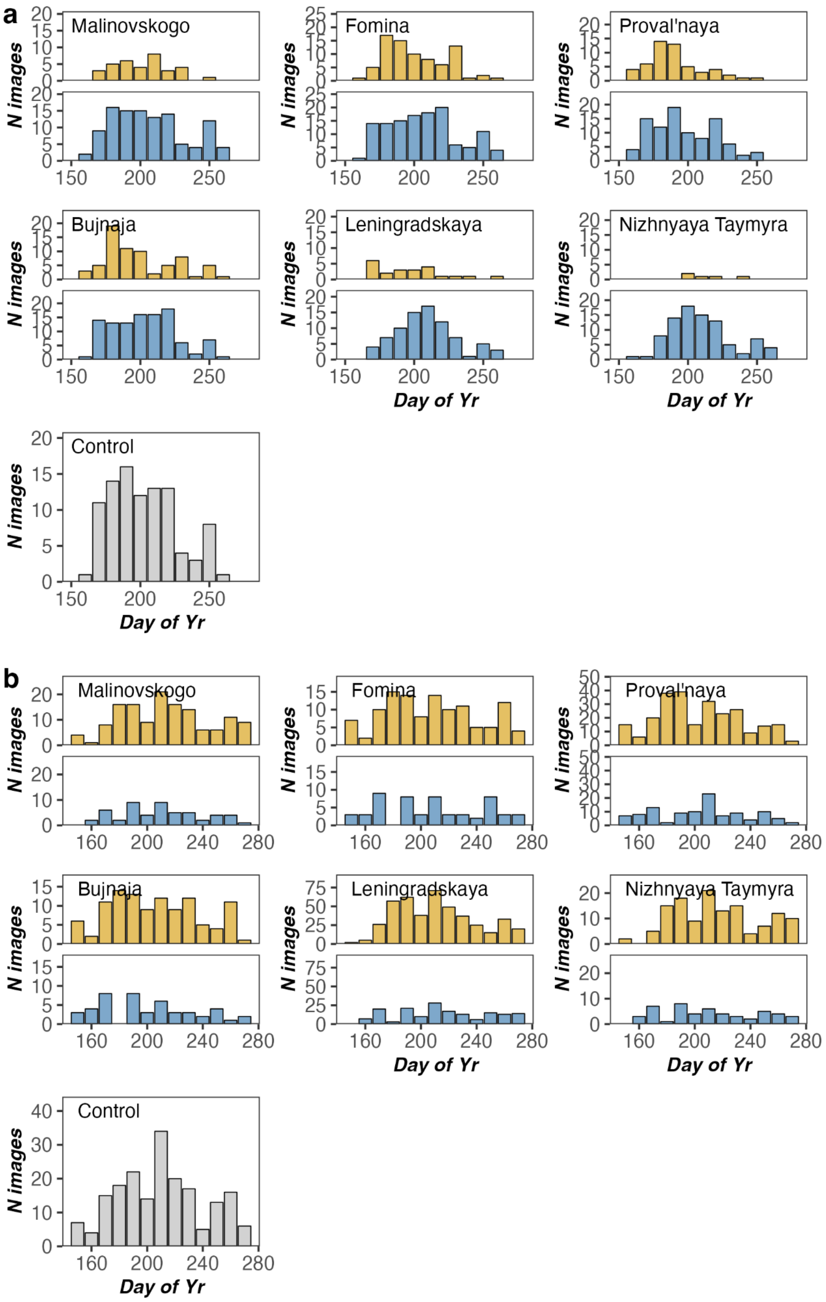

Fig. A1. Number of images for SSC analysis for rivers in the study area. Image dates for Landsat, a, and Sentinel-2, b, are aggregated into day-of-year bins that are 10 days wide. Pre- (blue) and post-slump (yellow) distributions are shown. Note that y-axis scales are different.

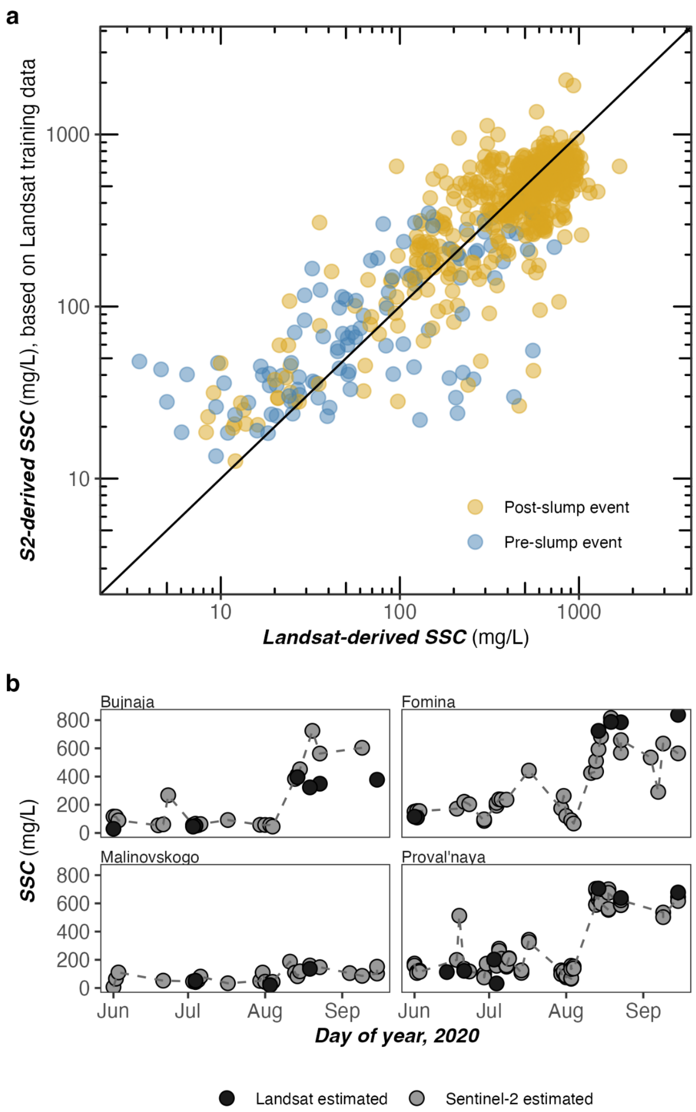

Fig. A2. Suspended sediment concentration estimated from Sentinel-2 data plotted against Landsat-derived SSC. a, SSC prediction model fit shows generally good agreement, with some scatter, particularly at low SSC values. Color of the symbols indicates whether the sample is from before or after the 2020 initiation of most thaw slumps in the study region. Landsat and Sentinel-2 samples are from the same day. b, Example timeseries from 2020 showing generally good agreement between SSC estimated from Sentinel-2 and Landsat and also highlights the relative temporal density of the Sentinel-2 record.

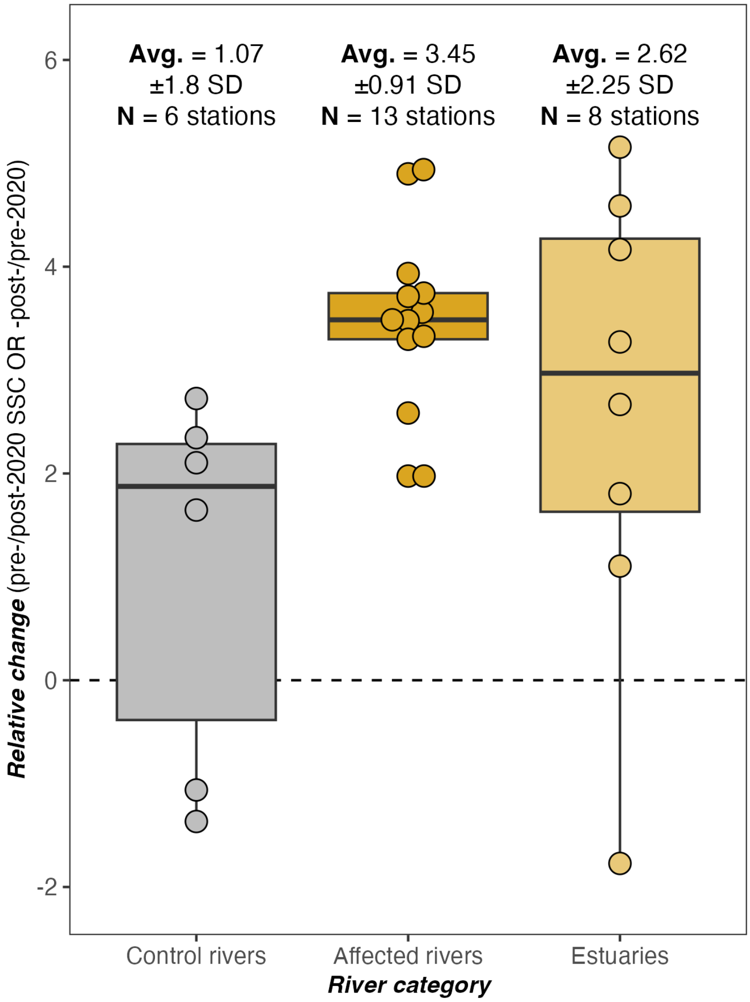

480 **Fig. A3. Changes to SSC relative to pre-slump for satellite sampling stations along control rivers (grey), rivers downstream of thaw slumps (orange), and estuaries (yellow). For rivers with SSC increase, relative change is calculated by dividing post-slump SSC by pre-slump SSC. Relative change for rivers with a decrease in SSC is calculated by dividing pre-slump SSC by post-slump SSC and multiplying by -1 to make the presentation symmetrical around 0 (no change).**

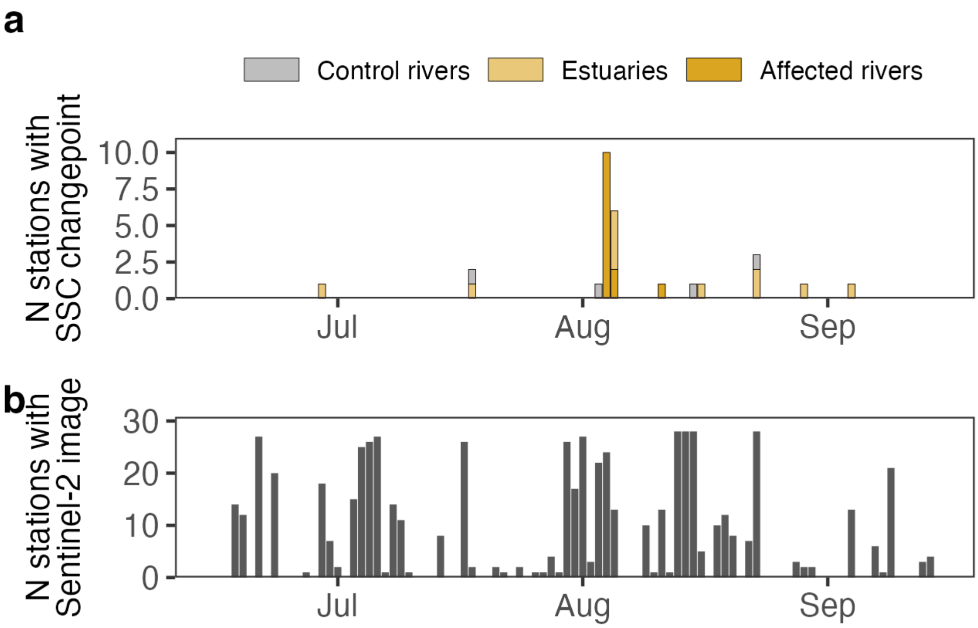

Fig. A4. Number of stations with a changepoint date for each date in the warm season in 2020 (a), colored by station designation, compared to the number of stations with an SSC measurement from Sentinel-2 for the same period in 2020. Change to higher SSC occurred coherently across the region, with 16 stations out of 24 non-control river stations registering the changepoint on Aug. 4th or 5th, 2020. Note that control stations are shown in both panels.

https://doi.org/10.5194/egusphere-2025-5691
Preprint. Discussion started: 8 December 2025

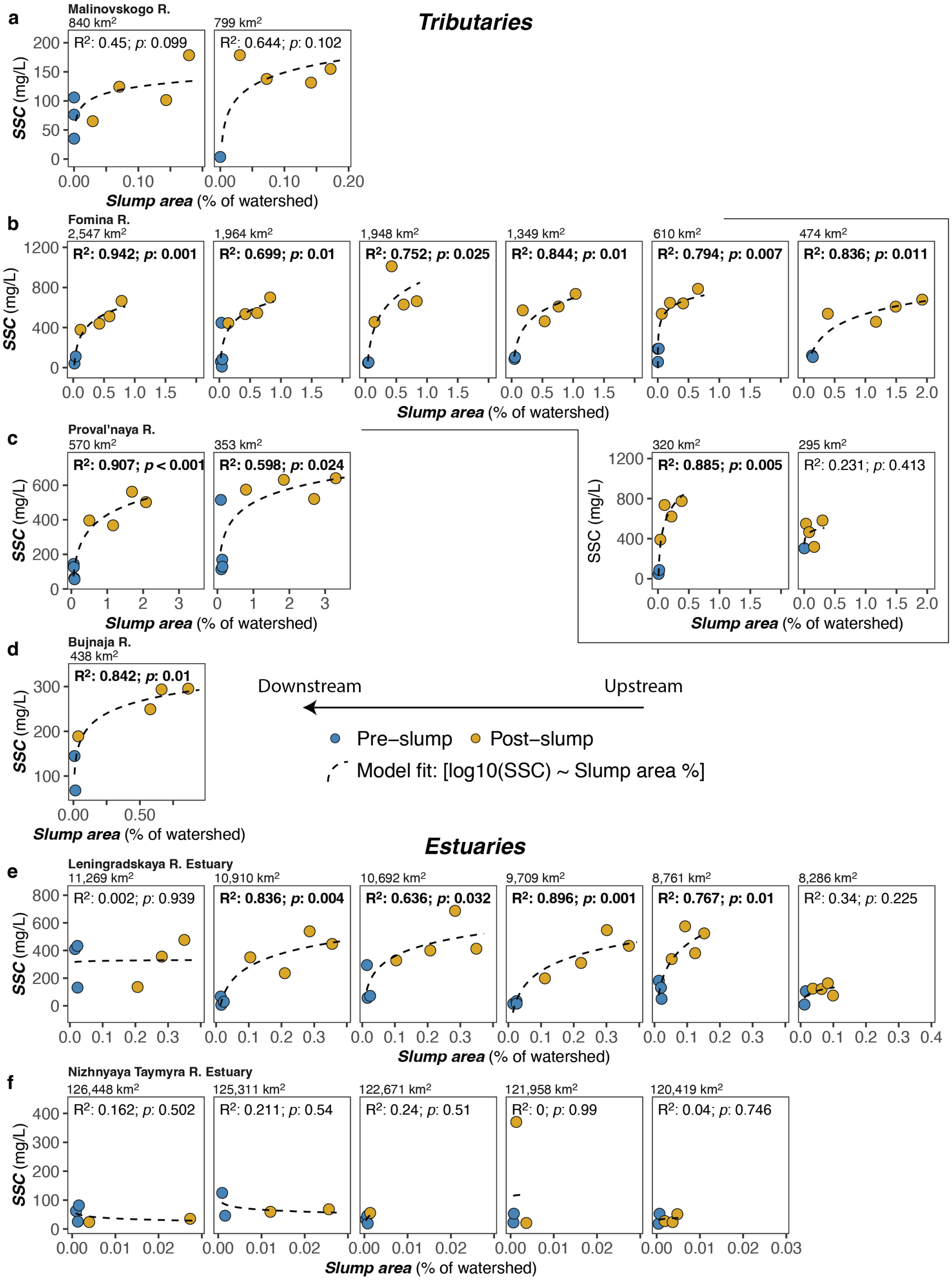

Fig. A5. SSC scales with upstream percent slump area for rivers affected by thaw slumps on the Taymyr Peninsula, Russia (pre-2020: blue symbols; post-2020: yellow symbols). Each satellite-based sampling station is shown on its own panel, with drainage area indicating watershed position. The dashed line on each panel is a least-squares fit relating SSC to the log-transformed percent slump area. The relationship R^2 and p-value is shown at the top of each panel, bolded if significant ($p < 0.05$).

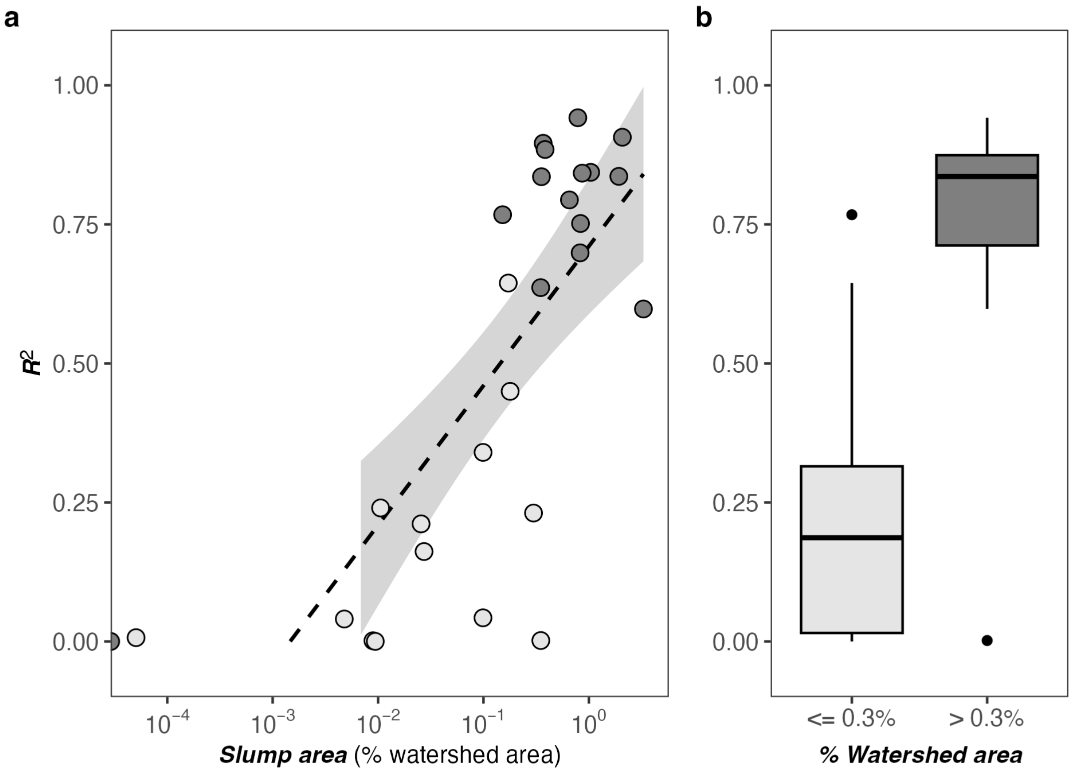

500 **Fig. A6. The variance in SSC explainable by percent slump area can increasingly be explained in watersheds with higher percent slump area. For slumps with percent slump area > 0.3% the median R^2 is > 0.8 and relationships are generally statistically significant ($p < 0.05$). Below a percent slump area of 0.3%, the relationship between percent slump area and SSC is generally not significant, indicating that other erosion and sediment transport processes are dominant.**

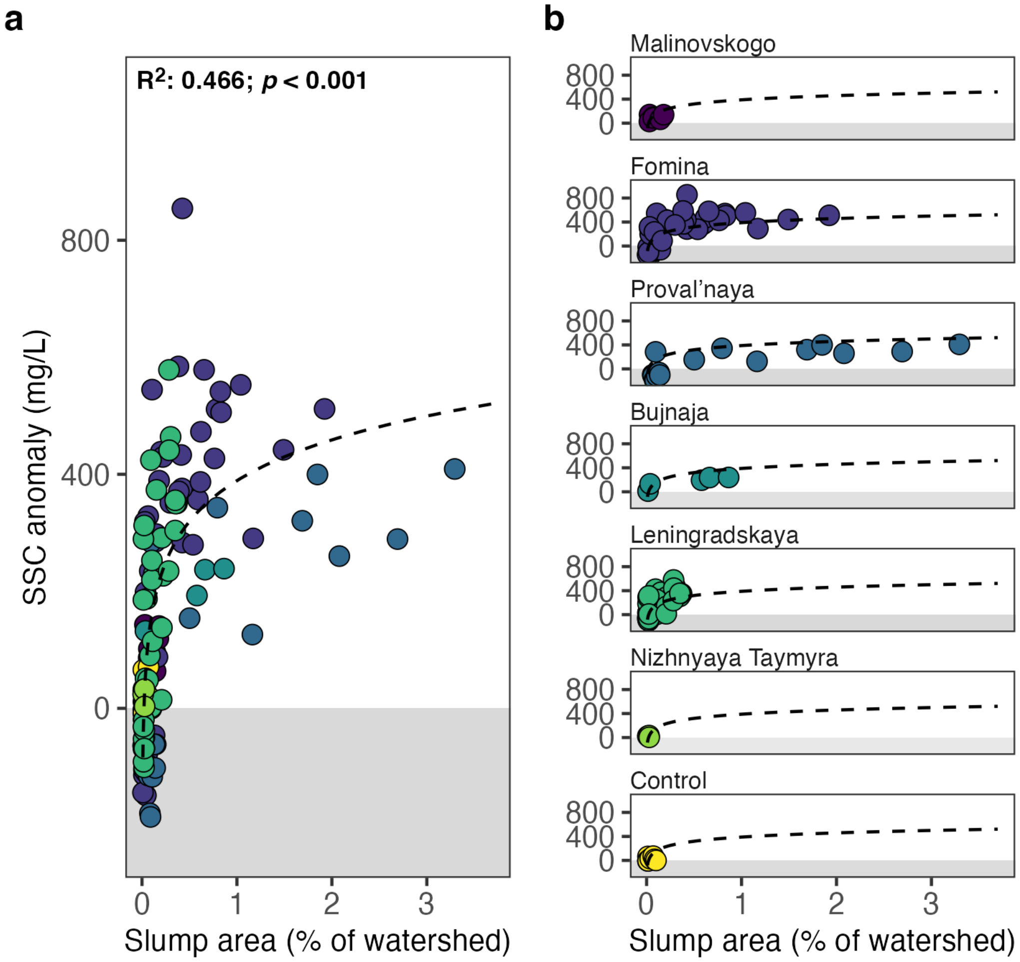

505

Fig. A7. Region-wide relationship between percent slump area and average annual SSC anomaly (mg/L). a, All observations from satellite sampling stations with percent slump area > 0.01%. The dashed line is the least squares fit relating SSC to the log-transformed percent slump area, incorporating these samples from all stations. The relationship R^2 and *p*-value is shown at the top of the panel. b, Observations of average annual SSC anomaly are shown for each individual river, including control rivers. The same fit from panel a is overlain on each river, showing the relative generality of this relationship across rivers in the study area. 510

https://doi.org/10.5194/egusphere-2025-5691
Preprint. Discussion started: 8 December 2025

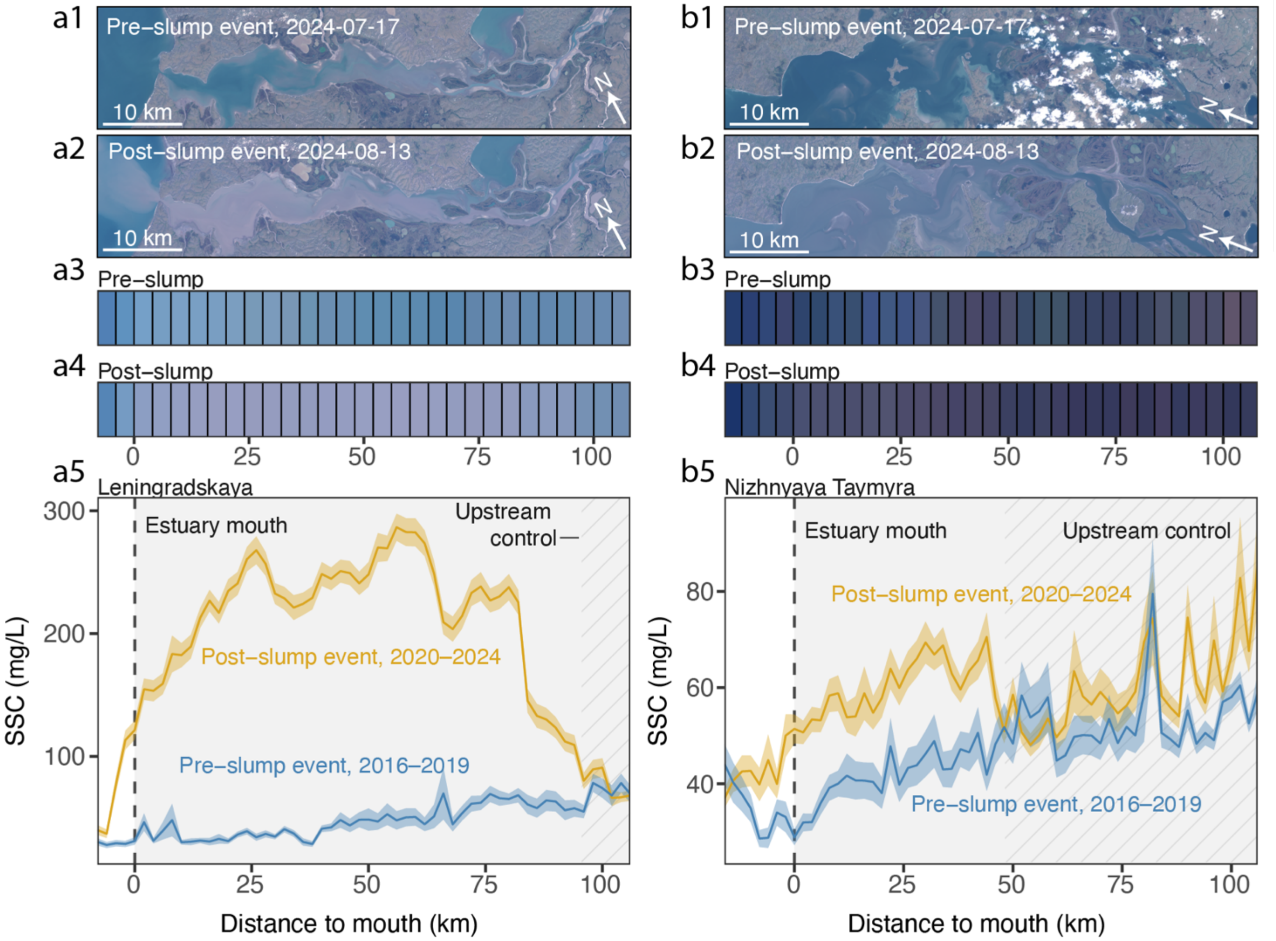

Fig. A8. Estuaries indicate peak sediment transport just downstream of slump-affected tributaries, with attenuation downstream of these inputs. The Leningradskaya R. Estuary (a) has more pronounced increases in SSC, likely due to its smaller size (11,269 km² at the mouth) than the Nizhnyaya Taymyra R. Estuary (b) (126,448 km² at the mouth) and thus higher percent slump area. Qualitative imagery analysis (a1–4; b1–4) shows limited SSC in estuaries pre-slump event in July 2020 and increased SSC immediately post-slump event in August 2020. Aggregate analysis of average Landsat image color every 4 km in the estuary (a3,4; b3,4) also indicates limited pre-slump estuarine SSC from 1984–2019 (darker colors), and elevated SSC post-slump from 2020–2024 (lighter colors), with particularly pronounced increase for the Leningradskaya R. Estuary. Quantitative SSC analysis based on Sentinel-2 images (c) shows attenuation in SSC near both estuary mouths, with peak SSC driven by tributary inputs.

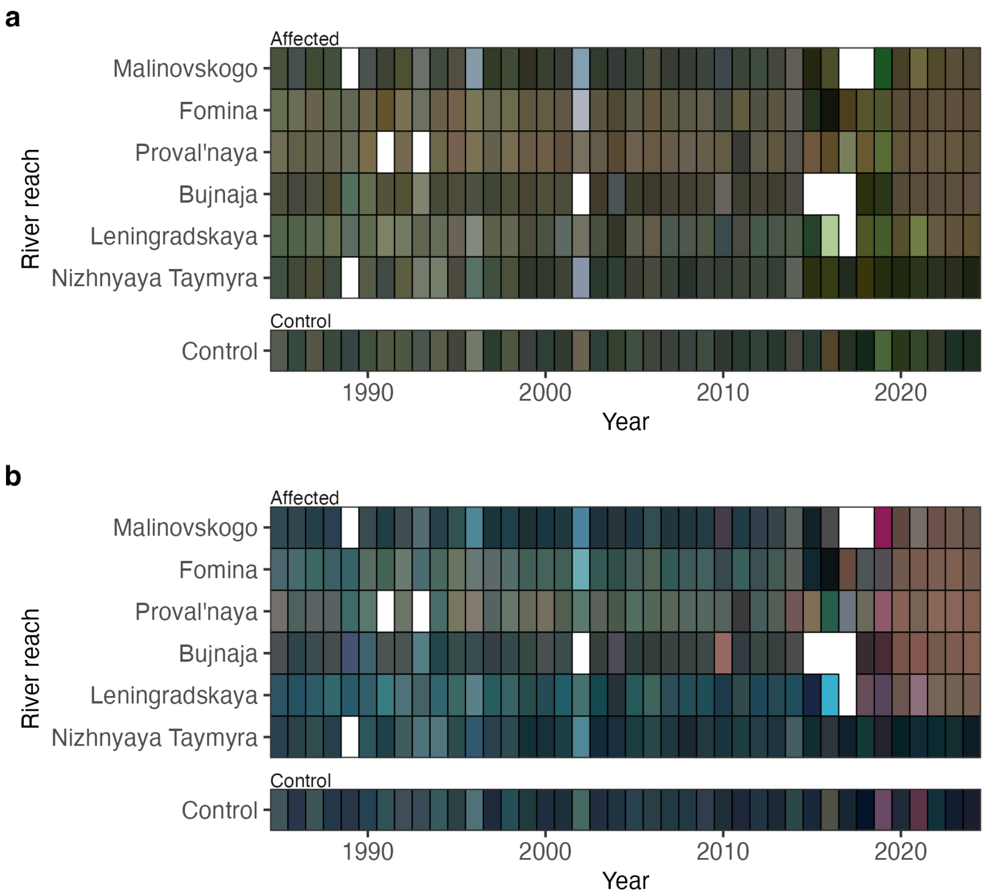

Fig. A9. River color changes following the 2020 Taymyr Peninsula thaw slump event, derived from Landsat surface reflectance data. a, True-color (Red-Green-Blue) and b, false-color (Near-infrared-Red-Green)

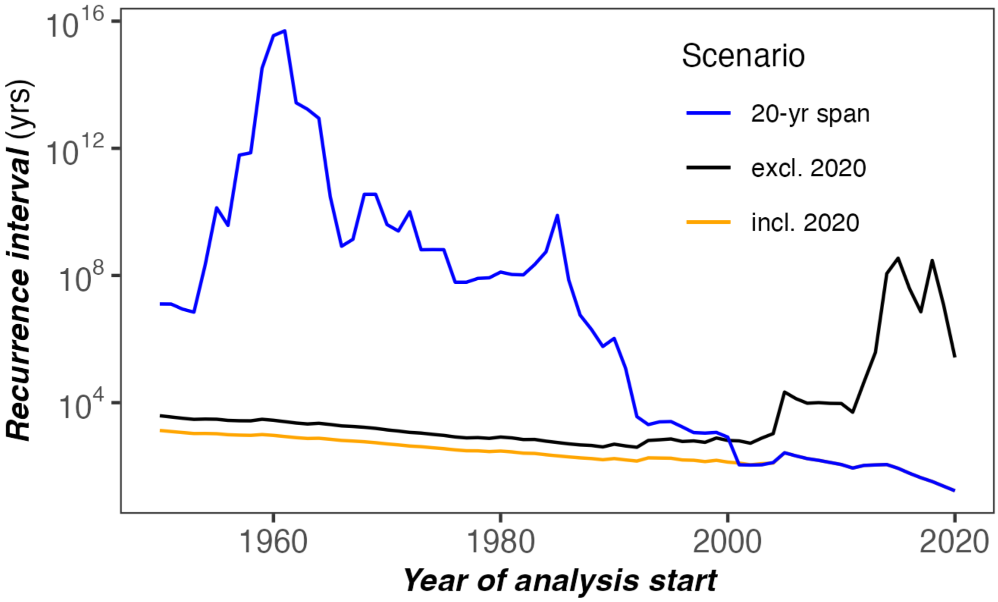

530 **Fig. A10. Recurrence interval calculation for different scenarios. In each scenario, the recurrence interval was calculated based on a range of years extending from the year of analysis start (x-axis) to 2024. Two scenarios are shown, one that includes 2020 in the calculation (orange line) and one that excludes 2020 from the calculation (black line).**

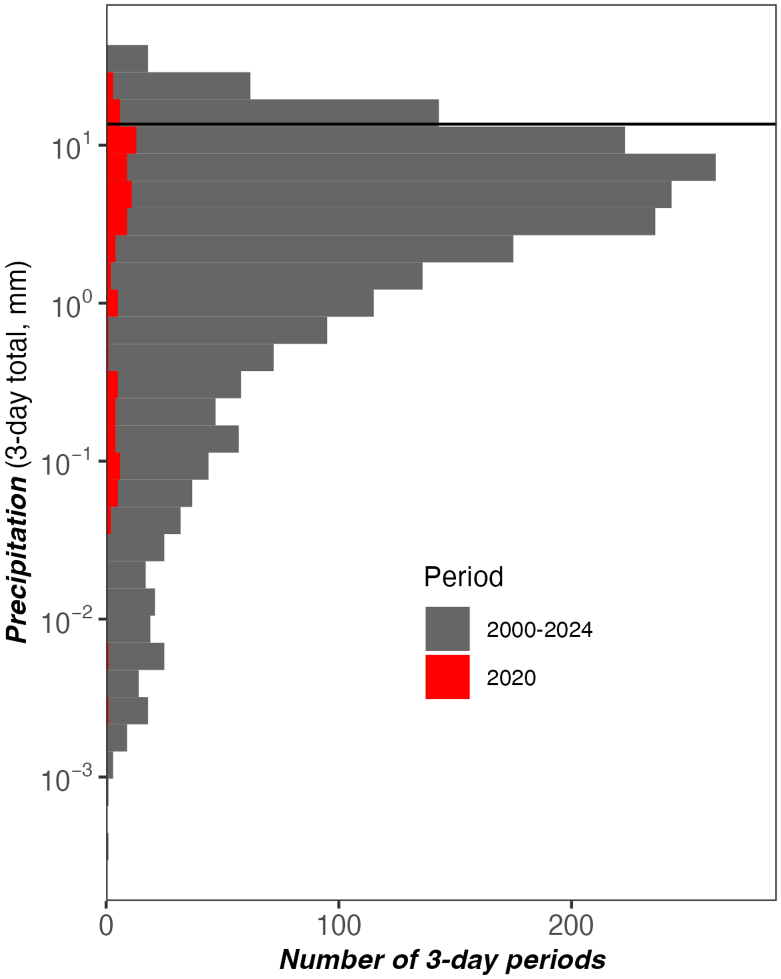

535 **Fig. A11. Distribution of precipitation during the warm season (June, July, and August) for two periods, 2020–2024 (grey) and 2020 (red), the year of thaw slump acceleration and sediment transport increase. The solid line indicates a three-day total precipitation of 14 mm, the amount that fell before a stepwise change in SSC for many rivers in the study area. Although uncommon, on average there are 8.3 warm-season days per year with a 3-day precipitation total of 14 mm or greater (n = 200 days, 2000–2024), and 1.2 days per year with a single-day total of 14 mm or greater (n = 28 days, 2000–2024).**

540

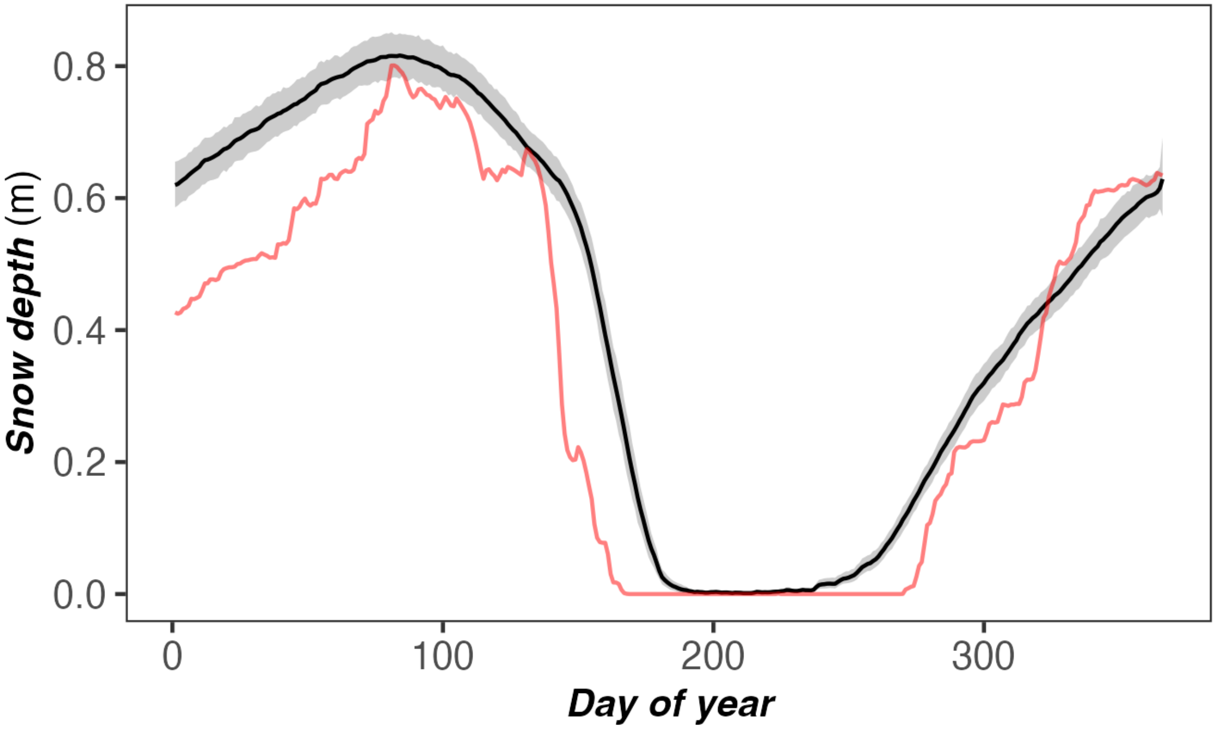

Fig. A12. Snow depth estimated by NASA ERA5 reanalysis data. Average from 1950–2024 is shown in black (grey shading indicates +/- 1 SD). The snow depth from 2020 is shown in red. 545

Author contribution

ED, CE, and CR conceptualized the study. ED and CE curated the data. ED managed data analysis, and wrote the original draft, which was reviewed and edited by CE and CR. ED and CR acquired funding.

Code availability

Code necessary for acquisition and processing of raw data, model training, and figure production is available at https://github.com/evandethier/arctic_rivers.

Data availability

Raw data used for these analyses are publicly available via NASA (Landsat) and ESA (Sentinel-2) public repositories. Data will be available as part of the permanent project archive at https://github.com/evandethier/arctic_rivers.

Competing interests

The authors declare that they have no conflict of interest.

Acknowledgements

River names were obtained from Open Street Map (https://www.openstreetmap.org/) and translated from Cyrillic to the Latin alphabet using Google Translate (https://translate.google.com/). Support for this research was provided by National Aeronautics and Space Administration (NASA) award 80NSSC23K1293.

References

Bernhard, P., Zwieback, S., and Hajnsek, I.: Accelerated mobilization of organic carbon from retrogressive thaw slumps on the northern Taymyr Peninsula, The Cryosphere, 16, 2819–2835, https://doi.org/10.5194/tc-16-2819-2022, 2022a.

Bernhard, P., Zwieback, S., Bergner, N., and Hajnsek, I.: Assessing volumetric change distributions and scaling relations of retrogressive thaw slumps across the Arctic, The Cryosphere, 16, 1–15, https://doi.org/10.5194/tc-16-1-2022, 2022b.

Burn, C. r. and Lewkowicz, A. g.: Canadian Landform Examples - 17 Retrogressive Thaw Slumps, Can. Geogr. Géographies Can., 34, 273–276, https://doi.org/10.1111/j.1541-0064.1990.tb01092.x, 1990.

Copernicus Climate Change Service, Climate Data Store: ERA5 hourly data on single levels from 1940 to present, 2023.

Dai, C., Ward Jones, M. K., van der Sluijs, J., Nesterova, N., Howat, I. M., Liljedahl, A. K., Higman, B., Freymueller, J. T., Kokelj, S. V., and Sriram, S.: Volumetric quantifications and dynamics of areas undergoing retrogressive thaw slumping in the Northern Hemisphere, Nat. Commun., 16, 6795, https://doi.org/10.1038/s41467-025-62017-0, 2025.

DeAngelis, A. M., Schubert, S. D., Chang, Y., Lim, Y.-K., Koster, R. D., Wang, H., and Collow, A. B. M.: Dynamical Drivers of the Exceptional Warmth over Siberia during the Spring of 2020, J. Clim., 36, 4837–4861, https://doi.org/10.1175/JCLI-D-22-0387.1, 2023.

Dethier, E. N., Renshaw, C. E., and Magilligan, F. J.: Toward Improved Accuracy of Remote Sensing Approaches for Quantifying Suspended Sediment: Implications for Suspended-Sediment Monitoring, J. Geophys. Res. Earth Surf., 125, e2019JF005033, https://doi.org/10.1029/2019JF005033, 2020.

Dethier, E. N., Renshaw, C. E., and Magilligan, F. J.: Rapid changes to global river suspended sediment flux by humans, Science, 376, 1447–1452, https://doi.org/10.1126/science.abn7980, 2022.

Dethier, E. N., Silman, M., Leiva, J. D., Alqahtani, S., Fernandez, L. E., Pauca, P., Çamalan, S., Tomhave, P., Magilligan, F. J., Renshaw, C. E., and Lutz, D. A.: A global rise in alluvial mining increases sediment load in tropical rivers, Nature, 620, 787–793, https://doi.org/10.1038/s41586-023-06309-9, 2023.

Erikson, C. M., Dethier, E. N., and Renshaw, C. E.: Seasonal dynamics of a coupled hillslope — river system in the Arctic revealed by semi-automated satellite image analysis, Remote Sens. Environ., 328, 114883, https://doi.org/10.1016/j.rse.2025.114883, 2025.

Fields, J., Kreisler, J., Dethier, E., Perrotti, J., and Renshaw, C.: Fluvial erosion linked to warming in the Canadian Arctic, Commun. Earth Environ., 6, 267, https://doi.org/10.1038/s43247-025-02234-z, 2025.

Geyman, E. C., Douglas, M. M., Avouac, J.-P., and Lamb, M. P.: Permafrost slows Arctic riverbank erosion, Nature, 634, 359–365, https://doi.org/10.1038/s41586-024-07978-w, 2024.

Hjort, J., Karjalainen, O., Aalto, J., Westermann, S., Romanovsky, V. E., Nelson, F. E., Etzelmüller, B., and Luoto, M.: Degrading permafrost puts Arctic infrastructure at risk by mid-century, Nat. Commun., 9, 5147, https://doi.org/10.1038/s41467-018-07557-4, 2018.

Ielpi, A., Lapôtre, M. G. A., Finotello, A., and Roy-Léveillée, P.: Large sinuous rivers are slowing down in a warming Arctic, Nat. Clim. Change, 13, 375–381, https://doi.org/10.1038/s41558-023-01620-9, 2023.

Jiao, C., Niu, F., He, P., Luo, J., and Yu, F.: Assessment of freeze-thaw erosion by retrogressive thaw slump on the Qinghai-Tibet Plateau combined with geophysical methods, Npj Nat. Hazards, 2, 46, https://doi.org/10.1038/s44304-025-00085-4, 2025.

Kokelj, S. V., Lacelle, D., Lantz, T. C., Tunnicliffe, J., Malone, L., Clark, I. D., and Chin, K. S.: Thawing of massive ground ice in mega slumps drives increases in stream sediment and solute flux across a range of watershed scales, J. Geophys. Res. Earth Surf., 118, 681–692, https://doi.org/10.1002/jgrf.20063, 2013.

Kokelj, S. V., Tunnicliffe, J., Lacelle, D., Lantz, T. C., Chin, K. S., and Fraser, R.: Increased precipitation drives mega slump development and destabilization of ice-rich permafrost terrain, northwestern Canada, Glob. Planet. Change, 129, 56–68, https://doi.org/10.1016/j.gloplacha.2015.02.008, 2015.

https://doi.org/10.5194/egusphere-2025-5691
Preprint. Discussion started: 8 December 2025

Kokelj, S. V., Kokoszka, J., van der Sluijs, J., Rudy, A. C. A., Tunnicliffe, J., Shakil, S., Tank, S. E., and Zolkos, S.: Thaw-driven mass wasting couples slopes with downstream systems, and effects propagate through Arctic drainage networks, The Cryosphere, 15, 3059–3081, https://doi.org/10.5194/tc-15-3059-2021, 2021.

Lantz, T. C. and Kokelj, S. V.: Increasing rates of retrogressive thaw slump activity in the Mackenzie Delta region, N.W.T., Canada, Geophys. Res. Lett., 35, https://doi.org/10.1029/2007GL032433, 2008.

Lewkowicz, A. G. and Way, R. G.: Extremes of summer climate trigger thousands of thermokarst landslides in a High Arctic environment, Nat. Commun., 10, 1329, https://doi.org/10.1038/s41467-019-09314-7, 2019.

Lininger, K. B. and Wohl, E.: Floodplain dynamics in North American permafrost regions under a warming climate and implications for organic carbon stocks: A review and synthesis, Earth-Sci. Rev., 193, 24–44, https://doi.org/10.1016/j.earscirev.2019.02.024, 2019.

Luo, W., Shen, F., He, Q., Cao, F., Zhao, H., and Li, M.: Changes in suspended sediments in the Yangtze River Estuary from 1984 to 2020: Responses to basin and estuarine engineering constructions, Sci. Total Environ., 805, 150381, https://doi.org/10.1016/j.scitotenv.2021.150381, 2022.

Maier, K., Bernhard, P., Ly, S., Volpi, M., Nitze, I., Li, S., and Hajnsek, I.: Detecting mass wasting of Retrogressive Thaw Slumps in spaceborne elevation models using deep learning, Int. J. Appl. Earth Obs. Geoinformation, 137, 104419, https://doi.org/10.1016/j.jag.2025.104419, 2025.

Newcombe, C. P. and Macdonald, D. D.: Effects of Suspended Sediments on Aquatic Ecosystems, North Am. J. Fish. Manag., 11, 72–82, https://doi.org/10.1577/1548-8675(1991)011%253C0072:EOSSOA%253E2.3.CO;2, 1991.

Perkins-Kirkpatrick, S. E. and Lewis, S. C.: Increasing trends in regional heatwaves, Nat. Commun., 11, 3357, https://doi.org/10.1038/s41467-020-16970-7, 2020.

Rantanen, M., Kämäräinen, M., Luoto, M., and Aalto, J.: Manifold increase in the spatial extent of heatwaves in the terrestrial Arctic, Commun. Earth Environ., 5, 570, https://doi.org/10.1038/s43247-024-01750-8, 2024.

Rodriguez, A. B., McKee, B. A., Miller, C. B., Bost, M. C., and Atencio, A. N.: Coastal sedimentation across North America doubled in the 20th century despite river dams, Nat. Commun., 11, 3249, https://doi.org/10.1038/s41467-020-16994-z, 2020.

Rowland, J. C., Schwenk, J. P., Shelef, E., Muss, J., Ahrens, D., Stauffer, S., Pilliouras, A., Crosby, B., Chadwick, A., Douglas, M. M., Kemeny, P. C., Lamb, M. P., Li, G. K., and Vulis, L.: Scale-Dependent Influence of Permafrost on Riverbank Erosion Rates, J. Geophys. Res. Earth Surf., 128, e2023JF007101, https://doi.org/10.1029/2023JF007101, 2023.

Slagle, A. L., Ryan, W. B. F., Carbotte, S. M., Bell, R., Nitsche, F. O., and Kenna, T.: Late-stage estuary infilling controlled by limited accommodation space in the Hudson River, Mar. Geol., 232, 181–202, https://doi.org/10.1016/j.margeo.2006.07.009, 2006.

Zhang, T., Li, D., East, A. E., Walling, D. E., Lane, S., Overeem, I., Beylich, A. A., Koppes, M., and Lu, X.: Warming-driven erosion and sediment transport in cold regions, Nat. Rev. Earth Environ., 3, 832–851, https://doi.org/10.1038/s43017-022-00362-0, 2022.